2014 年 2 月

碩士學位 論文

Surface Characteristics of Si-HA Film Coated Ti-30Nb-xTa Alloys by Electrochemical Deposition

朝鮮大學校 大學院

光技術工學科(光應用學專攻)

金 恩 實

Surface Characteristics of Si-HA Film Coated Ti-30Nb-xTa Alloys by Electrochemical Deposition

전기화학증착법을 이용하여 Si-HA가 증착된
Ti-30Nb-xTa 합금의 표면특성

2014年 2月 25日

朝鮮大學校 大學院

光技術工學科(光應用工學專攻)

金 恩 實

Surface Characteristics of Si-HA Film Coated Ti-30Nb-xTa Alloys by Electrochemical Deposition

指導敎授　崔 漢 喆

이 論文을 工學 碩士學位申請 論文으로 提出함

2013年 10月

朝鮮大學校 大學院

光技術工學科(光應用工學專攻)

金 恩 實

金恩實의 碩士學位論文을 認准함

委 員 張　南部大學校　　敎　授　姜 保 安　印

委　　員　朝鮮大學校　　敎　授　張 賢 鮮　印

委　　員　朝鮮大學校　　敎　授　崔 漢 喆　印

2013年 11月

朝鮮大學校 大學院

CONTENTS

LIST OF TABLES

LIST OF FIGURES

국 문 초 록

전기화학증착법을 이용하여 Si-HA가 증착된 Ti-30Nb-xTa 합금의 표면특성

김 은 실
지도교수: 최한철, 공학/치의학박사
광기술공학과 (광응용공학전공)
조선대학교 대학원

본 논문에서는, 전기화학증착법을 이용하여 Si-HA가 증착된 Ti-30Nb-xTa 합금의 표면특성을 연구하기 위하여 Ta의 함량을 조절하여 3 및 15 wt. %가 되도록 아크용해법을 이용하여 Ti-30Nb-xTa 삼원계을 제조하였다. 균질화 처리를 위해 1000 ℃에서 12시간 동안 열처리 한 후 급냉하여 디스크 형태로 시편을 사용하였다. 전기화학증착법을 이용하여 2.5 mM $Ca(NO_3)_2{\cdot}4H_2O$ + 1.4 mM $NH_4H_2PO_4$ + 0.1 mM $Na_2SiO_3{\cdot}9H_2O$ 전해질 용액에서 Si-HA를 석출 하였고, 이때 85 ℃의 전해질 온도에서 실시하였다. 전기화학증착법은 일반적인 3상의 전기화학셀을 이용하였으며, cyclic voltammetry (CV) 방법으로 실행하였다.

본 모든 시편의 표면은 FE-SEM, EDX, OM, XRD, 및 ATR-FTIR 등으로 분석하였다. 생체적합성을 평가하기 위하여 Si-HA 증착된 Ti-30Nb-xTa 합금 표면의 접촉각을 측정하여 다음과 같은 결과를 얻었다.

1. Ti-30Nb-xTa 합금은 Ta 함량이 증가할수록 결정입의 크기가 증가하였으며 X-선 회절 분석 결과 합금에서 Ta 함량이 증가할수록 더 높은 β 상 피크를 나타내었고 α″ + β상에서 β상으로 변하였다.
2. Ti-30Nb-xTa 합금에서 Si-HA는 침상구조에서 먼저 석출이 되어 판모양 구조에서 막대모양과 꽃모양의 구조로 변하였다. 또한 Si-HA는 싸이클이 증가함에 따라 막대모양으로 변하였다.
3. Si-HA가 증착된 Ti-30Nb-xTa 합금의 EDS 결과로부터 O, Ca, P, Si, Ti,

Nb, 및 Ta 의 원소가 검출되었으며, TF-XRD 결과, HA가 형성되었다. 또한 ATR-FTIR 분석결과, Si-HA에서 SiO_4^{4-} 이온이 형성되었다.

4. 접촉각 측정으로부터, Si-HA를 30 싸이클 동안 증착된 Ti-30Nb-xTa 합금은 처리하지 않은 합금과 Si-HA를 10 싸이클 동안 처리한 표면 보다 낮은 접촉각을 보였다.

결론적으로, Si-HA는 싸이클 횟수에 따라 표면에 형태가 변하였고, 낮은 접촉각을 보임으로써 Si-HA가 생체적합성을 개선시킬 수 있을 것으로 생각 된다.

Ⅰ. INTRODUCTION

Titanium (Ti) and Ti-6Al-4V ELI alloy (an α/β-type alloy), have been regarded as suitable structural biomaterials and are currently widely used for replacing failed hard tissues, such as artificial hip, shoulder and knee joints, and dental implants due to their excellent specific strength, corrosion resistance, and biocompatibility [1]. However, the use of the Ti-6Al-4V alloy in medicine is then a subject of controversy because aluminium ions released are suspected to be associated with long term health problems like neurological pathologies and vanadium oxide, V_2O_5, is also known to be cytotoxic [2]. Recently β-type Ti alloys have attracted attention for new biomedical shape memory and superelastic materials. The β-type Ti alloys are promising candidates for serving as bio-implant materials of human hard tissues (such as bone and teeth), because they have superior biocompatibility, excellent corrosion resistance, lower Young's modulus, higher specific strength and greater working properties in comparison with other metallic implant materials being in use nowadays [3, 4]. The selections of Ta and Nb as alloying additions to Ti are considered to the strongest β-stabilizers, effectively decreasing Young's modulus of Ti alloys [5, 6].

Surface modification is generally essential to improve the chemical bonding between Ti implant and bone tissues [7, 8]. Among the various attempts which have been made to improve the osseointegration, hydroxyapatite [$Ca_{10}(PO_4)_6(OH)_2$, HA] coating on Ti implants have shown good fixation to the host bone and increased bone ingrowth to the implant [9]. Whereas, the synthesized HA is a pure phase that is well established bone replacement material in orthopaedics and dentistry [10]. Among the various ion substitutions (Na, Mg, Zn, Sr, and Si) that occur at trace (< 1 wt. %) levels in natural bone [11], silicon plays an important role in bone mineralization and formation and is therefore used in a wide variety of medical implants and bone grafts [12].

According to the literature silicon substituted hydroxyapatite (Si-HA) is a highly promising material in the field of bioactive bone substitutes and bone tissue engineering [13]. Nowadays, Si-HA have recently been deposited through coating techniques such as plasma spray [14], biomimetic [15], magnetron co-sputtering [16], sol-gel [17] and electron beam physical vapor deposition (EB-PVD) [18]. However, there is a few research on Si-HA coating deposited by electrochemical deposition.

Therefore, in this study, surface characteristics of Si-HA film coated Ti-30Nb-xTa alloys by electrochemical deposition have been investigated using FE-SEM, EDS, XRD, ATR-FTIR, and wettability test.

Ⅱ. BACKGROUND

2.1. Structure and properties of Ti [19, 20]

Ti appears on the atomic number of 22, a fourth-row transition metal with an atomic weight of 47.88. At temperatures up to 882 ℃, pure Ti exists as a hexagonal close-packes atomic structure (α phase). Above that temperature, the structure is body-centered cubic (β phase). The metal has a high melting point (1665 ℃). The physical properties of Ti are listed in Table 1. The atomic unit cells of the hexagonal close packed (hcp) α-Ti and the body-centered cubic (bcc) β-Ti are schematically shown in Fig. 1 with their most densely packed planes and directions highlighted. The existence of the two different crystal structures and the corresponding allotropic transformation temperature is of central importance since they are the basis for the large variety of properties achieved by Ti alloys.

Table 1. Summary of physical properties of pure Ti

Property	Value
Atomic number	22
Atomic mass (g/mol)	47.90
Density (g/cm^3)	4.51
Melting temperature (℃)	1665
Boiling temperature (℃)	3260
Transformation temperature (℃)	882
Discovered by	William Gregor in 1791

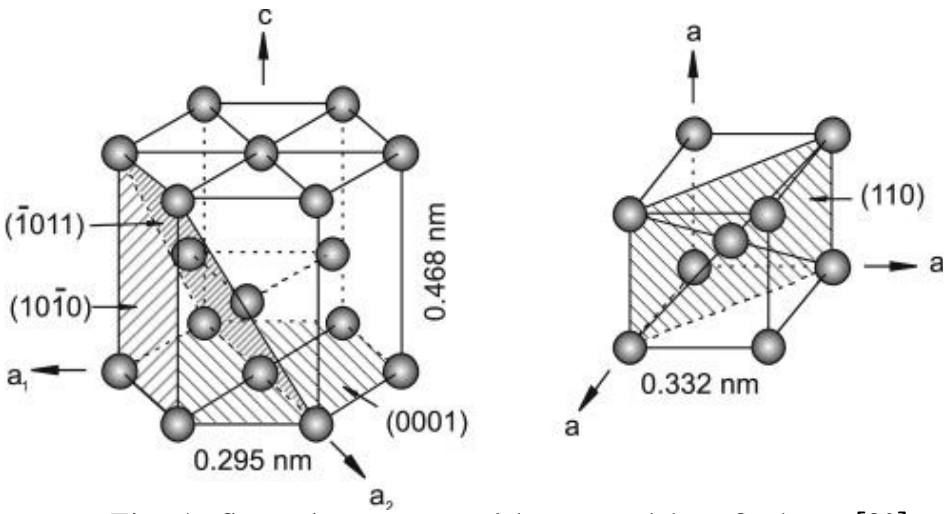

Fig. 1. Crystal structure of hcp α and bcc β phase [20].

2.1.1 Mechanical properties Ti alloys [21, 22]

The mechanical properties of Ti alloy are hardness, tensile strength, elastic modulus and elongation. The strength of the Ti alloys is very close to that of 316 L SS, and its density is 55 % less than steel, hence, when compared by specific strength (strength per density), the titanium alloys outperform any other implant material. Commercially pure (CP) Ti materials and some of its important alloys employed in the field of biomedical devices along with their mechanical properties are listed in Table 2. Ti-based alloys that have a high coefficient of friction can lead to formation of wear debris that result in inflammatory reaction causing pain and loosening of implants due to osteolysis. Owing to the above-mentioned limitations of the first generation materials listed in Table 2, the service period of the implants made out of them has been restricted to 10 - 15 years. This has interested biomedical researchers to develop an optimized prosthesis that mimics human bone. This has led to the development of low modulus beta titanium alloys that consist of compatible alloying additions and have modulus closer to that of bone which is discussed in detail in a later section. The low elastic modulus alloys that are currently under research with great interest are given in Table 2. The mechanical, wear and corrosion resistance of a material are largely determined by its microstructure. Ti alloys are privileged in a sense that a wide spectrum of microstructures is possible depending upon alloy chemistry and thermomechanical processing.

Table 2. Mechanical properties of biomedical Ti alloys [21]

Material	Standard	Modulus (GPa)	Tensile strength (Mpa)	Alloy type
First generation biomaterials (1950–1990)				
Commercially pure Ti (Cp grade 1–4)	ASTM 1341	100	240–550	α
Ti–6Al–4V ELI wrought	ASTM F136	110	860–965	α + β
Ti–6Al–4V ELI Standard grade	ASTM F1472	112	895–930	α + β
Ti–6Al–7Nb Wrought	ASTM F1295	110	900–1050	α + β
Ti–5Al–2.5Fe	–	110	1020	α + β
Second generation biomaterials (1990-till date)				
Ti–13Nb–13Zr Wrought	ASTM F1713	79–84	973–1037	Metastabe β
Ti–12Mo–6Zr–2Fe (TMZF)	ASTM F1813	74–85	1060–1100	β
Ti–35Nb–7Zr–5Ta (TNZT)		**55**	596	β
Ti–29Nb–13Ta–4.6Zr	–	65	911	β
Ti–35Nb–5Ta–7Zr–0.40 (TNZTO)		66	1010	β
Ti–15Mo–5Zr–3Al		82		β
Ti–Mo	ASTM F2066			β

2.1.2 β-Ti alloy [21, 23-27]

β-Ti alloys are the most versatile class of Ti alloys. They offer the highest strength to weight ratios and very attractive combinations of strength, toughness, and fatigue resistance at large cross sections. Some of the disadvantages compared to α + β alloys are increased density, a rather small processing window, and higher cost (Table 3). Further, Nb, Zr, Mo, and Ta are the most suitable alloying elements that can be added to decrease the elastic modulus of β-Ti without compromising the strength. It has been exhibited that addition of these alloying elements up to certain weight percentage decreases the elastic modulus, beyond which increase in elastic modulus is noted which is due to ω phase formation and precipitation of a on aging. It is also interesting to note that these elements fall into the category of non-toxic elements, which make them more suitable for implant applications. Based on these considerations the biomedical Ti alloys developed recently consist mainly of Ti, Nb, Ta and Zr. The mechanical properties of β-Ti alloy are shown in Table 4.

Table 3. Advantages and disadvantages of β-Ti alloys [23]

Advantages	*Disadvantages*
– high strength-to-density ratio	– high density
– low modulus	– low modulus
– high strength/high toughness	– poor low and high temperature properties
– high fatigue strength	– small processing window (some alloys)
– good deep hardenability	– high formulation cost
– low forging temperature	– segregation problems
– strip producible – low-cost TMP* (some alloys)	– high springback
– cold formable (some alloys)	– microstructural instabilities
– easy to heat treat	– poor corrosion resistance (some alloys)
– excellent corrosion resistance (some alloys)	– interstitial pick up
– excellent combustion resistance (some alloys)	

* TMP: thermomechanical processing

Table 4. Mechanical properties of β-Ti alloys [21]

Alloying addition	Tensile strength (Mpa)	0.2% Proof stress (Mpa)	Elongation (%)	Reduction in area (%)	Elastic modulus (Gpa)
Ti–30Nb–XTa–5Zr					
0Ta–20Ta	698–823	572–798	19.3–43.8 (decreases with increase in Ta)	51.3–73.0 (decreases with increase in Ta)	74.8–85.2 (decreases with increase in Ta)
Ti–XNb–Ta–5Zr					
20Nb–35Nb	742–806 (decreases with increase in Nb)	704–779 (decreases with increase in Nb)	11.6–22.6	19.0–62.4	–
Ti–XNb–13Ta–4.6Zr					
29Nb–39Nb	715	590	15	–	–
	612	600	22	–	–
Ti–35Nb–7Zr–5Ta–XO					
0.0 O–0.68	590–1074	–	21–27	47–69	

2.2. Surface treatment for implant materials [25]

The surface of an implant needs modification to optimize the properties of the implant and to maximize its bioactivity when interfacing with natural tissue. The biological characteristics of implants can be enhanced by adding material with desired properties, changing the composition or removing unwanted material from the implant surface. These methods are known as surface treatments or modifications, and can be classified into four categories: mechanical, physical, chemical and biochemical surface modifications. Machining, grinding, polishing and blasting are mechanical surface modifications. Physical surface treatments include thermal spraying, physical vapour deposition, ion implantation and deposition, and glow discharge plasma treatment. Chemical surface modifications include chemical treatment (acid, hydrogen peroxide, alkaline), anodic oxidation, the sol - gel process and chemical vapour deposition. A number of techniques have been specifically introduced for Ti and its alloys, such as silanized titania, photochemistry, self-assembled monolayers, protein resistance and protein immobilization.

2.2.1 Electrochemical methods

Electrochemical methods are increasingly being used for the preparation of thin films and coatings. The electrochemical methods has attracted considerable attention recently, because of its low temperature and cost, the control of coating thickness and chemical composition, and the ability to coat irregular morphology surface. It is based on an electrode reaction induced pH jump effect. When a current passes through an electrolytic cell, electrons are injected into the solution through cathodic reactions, and drawn out through anodic reactions. The nature of the reactions depends on the electrode potential and the solution conditions. At the cathode, some common reactions are:

$$2H^+ + 2e \rightarrow H_2\uparrow \quad \text{(discharge of proton)}$$

$$2H_2O + 2e \rightarrow 2OH^- + H_2\uparrow \quad \text{(reduction of molecular water)}$$

$$O_2\ (aq) + 2H_2O + 4e \rightarrow 4\ OH^- \quad \text{(reduction of dissolved oxygen)}$$

All these reactions can increase the pH of the solution adjacent to the cathode, because of either consuming acid or generating base. In a solution containing Ca^{2+} and phosphate species, the local pH jump drives hydrogenphosphate anions to dissociate and, when the pH reaches a critical point, causes calcium phosphate to crystallize on the cathode to form a coating.

2.3. Silicon substituted hydroxyapatite

2.3.1 Hydroxyapatite [26-28]

Hydroxyapatite [HA; $Ca_{10}(PO_4)_6(OH)_2$] is the most stable, the most dense and the most insoluble of the CaPs. From a chemical and structural point of view it is the material most similar to the mineral component of bones and teeth. HA can be easily prepared in aqueous solution. Apatites, as well as other CaPs, can also be obtained as the result of the transformation of more soluble, metastable phosphates in a wet environment. The main methods of preparation of CaPs are summarized in Table 5.

The hexagonal structure contains two different cation sites, Ca(Ⅰ) and Ca(Ⅱ), but only one phosphate environment (Ca(I), Ca(Ⅱ) are used for stoichiometric apatite; M(I), M(Ⅱ) are the general symbols for substituted apatites. The structure can be roughly described as a phosphate assembly crossed by parallel channels filled by OH^- ions and parallel to the crystallographic c-axis (Fig. 5). The channel walls are formed of Ca(Ⅱ) atoms arranged in staggered triangular arrays. Ca(Ⅰ) atoms have a different environment and are positioned in columns parallel to the OH^- channels. A unit

cell accommodates a formula unit $Ca_{10}(PO_4)_6(OH)_2$. Among the 10 cations, the 4 Ca(I)s are tightly bonded to 6 oxygens and less strongly to the other 3 oxygens (mean Ca(I)-O distance 0.255 nm), whereas the 6 Ca(Ⅱ) atoms are surrounded by 7 oxygens (mean Ca(Ⅱ)-O distance 0.245 nm). Ca(I) atoms are strictly aligned in columns and any small change in the metal-oxygen interactions affects the entire lattice. However, the Ca(Ⅱ) atoms belonging to consecutive layers are staggered, allowing random local misplacements without compromising the whole structure. As a consequence, cations smaller than Ca or also low concentrations of slightly larger cations are preferably accommodated in site Ca(I) where stronger interactions are present, while larger cations should be accommodated in position Ca(Ⅱ), even at high concentrations.

When a conducting surface is cathodically polarized in Ca and P containing solutions, different types of calcium phosphate depositions could occur depending on the pH condition. Brushite type deposit is expected in a relatively lower pH condition following the reaction:

$$Ca^{2+} + HPO_4^{2-} \rightarrow CaHPO_4 \qquad (1)$$

When the hydroxyl concentration increases, the acid phosphates are completely converted to phosphates by reaction (2):

$$HPO_4^{2-} + OH^- \rightarrow PO_4^{3-} + H_2O \qquad (2)$$

When The reactions (1) and (2) are basically chemical reactions. From these reactions, it can be observed that formation of the sufficient quantity of hydroxyls ions is necessary for deposition of HA according to the reaction (3):

$$10Ca^{2+} + 6PO_4^{3-} + 2OH^- \rightarrow Ca_{10}(PO_4)_6(OH)_2 \qquad (3)$$

Table 5. Properties of the biologically relevant phosphates [26]

Abbreviation	Formula	Name (mineral)	Ca/P ratio	pK_{sp} (25 °C)[a]	pH stability[a]	Main preparation methods	Occurrence in biological tissues
HA	$Ca_{10}(PO_4)_6(OH)_2$	Hydroxyapatite	1.67	116.8	9.5–12	(i) Titration of $Ca(OH)_2$ with H_3PO_4 (ii) Dropwise addition of HPO_4^{2-} solution to Ca^{2+} solution, pH > 9 (iii) Hydrolysis from other phosphates	Bone, dentin, enamel, dental calcifications, urinary stones, atherosclerotic plaques
OCP	$Ca_8H_2(PO_4)_6{\cdot}5H_2O$	Octacalcium phosphate	1.33	96.6	5.5–7.0	Dropwise addition of $Ca(Ac)_2$ to $HPO_4^{2-}/H_2PO_4^-$ solutions at 60 °C, pH 5	Dental and urinary calculi
β-TCP	$Ca_3(PO_4)_2$	β-Tricalcium phosphate (whitlokite)	1.5	28.9	[b]	(i) Solid-state reaction of $CaCO_3$ and DCPD at 900 °C (ii) Thermal conversion of CDHA	Dental and urinary calculi, soft-tissue deposits, artritic cartilage, usually present as β-TCMP
α-TCP	$Ca_3(PO_4)_2$	α-Tricalcium phosphate	1.5	25.5	[b]	Heat treatment of β-TCP at 1300 °C	Not found
ACP	$Ca_x(PO_4)_y{\cdot}nH_2O$	Amorphous calcium phosphate	1.2–2.2	[c]	[b]	Fast mixing of Ca^{2+} and HPO_4^{2-} solutions, RT	Soft-tissue calcifications
MCPM	$Ca(H_2PO_4)_2{\cdot}H_2O$	Monocalcium phosphate monohydrate	0.5	1.14	0–2	Titration of H_3PO_4 with $Ca(OH)_2$ in strong acidic environment	Not found
MCPA	$Ca(H_2PO_4)_2$	Anhydrous monocalcium phosphate	0.5	1.14	[b]	Heat treatment of MCPM at T > 100 °C	Not found
DCPD	$CaHPO_4{\cdot}2H_2O$	Dicalcium phosphate dihydrate (brushite)	1.0	6.59	2–6	Dropwise addition of a Ca^{2+} solution to a HPO_4^{2-} solution at 60 °C, pH 4	Dental calculi, urinary stones chondrocalcinosis
DCPA	$CaHPO_4$	Anhydrous dicalcium phosphate (monetite)	1.0	6.90	[b]	Heat treatment of DCPD at T > 100 °C	Not found
TTCP	$Ca_4(PO_4)_2$	Tetracalcium phosphate	2.0	38–44	[b]	Solid-state reaction of DCPA with $CaCO_3$ at high T	Not found
CDHA	$Ca_{10-x}(HPO_4)_x(PO_4)_{6-x}(OH)_{2-x}$	Calcium-deficient hydroxyapatite	1.5	85.1	6.5–9.5	Hydrolysis of ACP or α-TCP	Not found

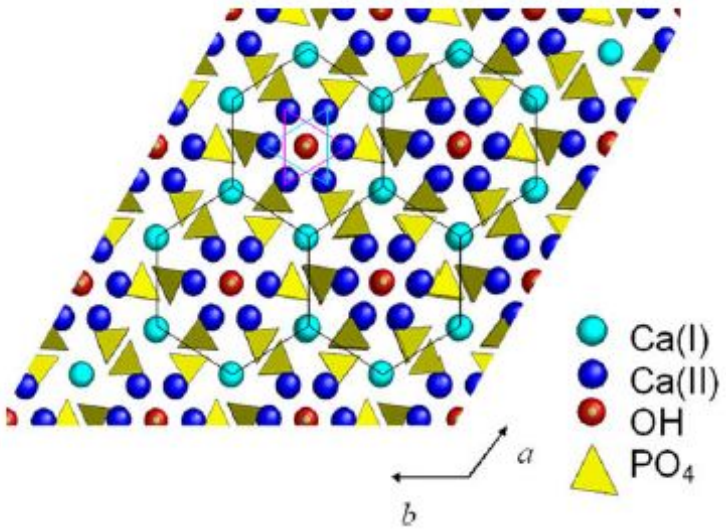

Fig. 2. A view of the HA structure along the c-axis [26].

2.3.2 Silicon in Body [29, 30]

Si is known to be essential as a trace element in biological processes. In particular, it has been reported to have a specific metabolic role connected to bone growth. As a consequence, Si-substituted HA have attracted the interest of many scientists because Si incorporation is considered to be a promising way to improve the bioactivity of HA-based biomaterials. The studies on material synthesized via an aqueous precipitation reaction are limited to Si-substituted HA (Si-HA), whereas most results have been derived from the products of sintering of apatites precipitated at low temperature. The amount of Si which can be incorporated into HA seems to be limited to a maximum of 5 wt. %, and amounts around 1 wt. % have been suggested to be enough to elicit important bioactive improvements.

Si plays a very important role at the microstructural level since it is responsible of the increase of the amorphous phase as well as of the reduction of the HA mean crystallite size (i.e. the mean size of coherently scattering domains). Si substitution influences the material surface by generating a more electronegative surface, by creating a finer microstructure, and then by increasing solubility. The increased bioactivity of Si-substituted HA with respect to HA could be related to the increased number of defects, in particular those involving grain boundaries, that have been suggested to be the starting point of in vivo dissolution.

2.3.3 Silicon substituted hydroxyapatite [31-34]

Recent Synthetic hydroxyapatite is similar to dental and bone mineral has good bioactivity and biocompatibility in biomedical applications. The synthesis and characterization of Si substituted HA (Si-HA) and Si substituted α -tricalcium phosphate (Si-α-TCP) has been the focus of many research efforts. Both Si-HA and Si-TCP based materials exhibit enhanced bone apposition, bone in-growth and cell-mediated degradation in comparison to stoichiometric HA controls. The synthesis of Si-HA and Si-α-TCP has focused on wet chemical methods where Si is introduced as a chemical carrier such as tetra ethyl or propyl ortho-silicate (TEOS or TPOS), Si Ⅳ acetate ($Si(COOCH_3)_4$), or as some form of nano-particulate silica during the precipitation or firing of an amorphous CaP or nanocrystalline HA.

Although the first additive used as silicon source in electrolytes is SiO_3^{2-}, silicon ions may be incorporated into HA in the form SiO_4^{4-} rather than SiO_3^{2-}. At pH value of 6, the SiO_3^{2-} may have reactions in aqueous solution as follows:

$$H_2O + SiO_3^{2-} \rightarrow H_2SiO_4^{2-} \quad (1)$$

$$H_2SiO_4^{2-} \rightarrow H^+ + HSiO_4^{3-} \quad (2)$$

$$HSiO_4^{3-} \rightarrow H^+ + SiO_4^{4-} \quad (3)$$

When a voltage is applied, cathodic reactions (4) - (7) occur during the deposition process:

$$2H^+ + 2e^- \rightarrow H_2 \quad (4)$$

$$2H_2O + 2e^- \rightarrow H_2 + 2OH^- \quad (5)$$

$$H_2PO_4^- + OH^- \rightarrow H_2O + HPO_4^{2-} \quad (6)$$

$$HPO_4^{2-} + OH^- \rightarrow H_2O + PO_4^{3-} \quad (7)$$

Reactions (1) - (3) transform SiO_3^{2-} to SiO_4^{4-} in solution. Reactions(4) - (5) yield OH^- ions which increase the pH and the degree of supersaturation relative to HA at the vicinity of titanium substrate. Reactions (6) - (7) yield PO_4^{3-} ions. As a result, Si-HA crystals are deposited on Ti substrates through the following reaction:

$$10Ca^{2+} + (6-\chi)PO_4^{3-} + \chi SiO_4^{4-} + (2-\chi)OH^- \quad (8)$$
$$\rightarrow Ca_{10}(PO_4)_{6-\chi}(SiO_4)_\chi(OH)_{2-\chi}$$

In the preparation reaction, SiO_4^{4-} is supposed to substitute PO_4^{3-} in the lattice, as shown in Fig.6. Accordingly, a portion of hydroxyl group would be lost to retain charge balance within the molecule, thus resulting in vacancy at the position of the hydroxyl group.

Below a limiting Si concentration, single-phase Si substituted forms of HA and α-TCP share the same crystallographic space groups as their stoichiometric counterparts, with characteristic changes to lattice parameters occurring with Si substitution. The space groups and lattice parameters of HA, Si-HA, α-TCP and Si-α-TCP are summarized in Table 6.

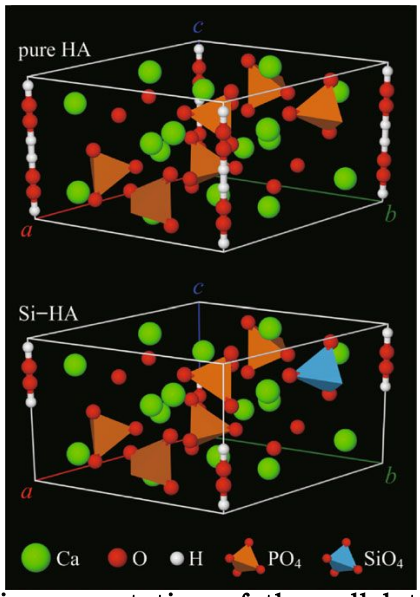

Fig. 3. Schematic presentation of the cell lattice comparison between pure HA and Si-HA [31].

Table 6. Space groups and lattice parameters of the biologically relevant phosphates [32]

Phase	Space group	Lattice parameters
HA	$P6_3/m$	$a = b = 9.4238(9)$ Å, $c = 6.8854(6)$ Å
Si-HA	$P6_3/m$	$a = b = 9.4082(1)$ Å, $c = 6.8828(1)$ Å
α-TCP	$P2_1/a$	$a = 12.887(2)$ Å, $b = 27.280(4)$ Å, $c = 15.219(2)$ Å, $\beta = 126.20(1)^\circ$
Si-TCP	$P2_1/a$	$a = 12.863(4)$ Å, $b = 27.357(9)$ Å, $c = 15.232(4)$ Å, $\beta = 126.3(1)^\circ$
Si-α-TCP (0.87 wt% Si)	$P2_1/a$	$a = 12.875(1)$ Å, $b = 27.372(2)$ Å, $c = 15.225(1)$ Å, $\beta = 126.38(1)^\circ$

Ⅲ. MATERIALS AND METHODS

3.1. Preparation of Ti-30Nb-xTa alloys

The Ti-30Nb-xTa (x = 0, 3, and 15 wt. %) ternary alloys were prepared from Ti (Grade 4, G&S Titanium, USA), Nb and Ta (99.95%, Kurt J. Lesker Co., USA), using controlled addition of Ta. The Ti-30Nb-xTa ingots were fabricated by using an arc-melting vacuum furnace (SVT, KOREA), with over 10 successive times of melting for individual specimens to improve the chemical homogeneity. Sponge Ti was initially melted in the chamber to serve as an oxygen scavenger to minimize the residual oxygen level before melting the prepared alloy. The ingots of Ti-30Nb-xTa alloy were obtained in the form of rod with about length of 60 mm and diameter of 10 mm, and ingots were approximately 20 g in weight. The Ti-30Nb-xTa ingots were subsequently further homogenized in a vacuum furnace (Model MSTF-1650, MS Eng, Korea) for 12 h at 1000 ℃ in an Ar atmosphere, followed by quenching in 0 ℃ water. Individual specimens having 2.5 mm thickness and 10 mm diameter were cut from the ingot, using a diamond saw (Accutom-5, Struers, Denmark). The sliced samples were mechanically abraded with SiC and then polished to 1 ㎛ using by Al_2O_3 suspension, and then ultrasonically cleaned in acetone and distilled water and finally dried in air.

3.2. Analysis of surface characteristics for Ti-30Nb-xTa alloys

To investigate the microstructure, the ternary titanium alloys were chemically etched in Keller's solution (20 mL H_2O + 5 mL HCl + 3 mL HNO_3 + 2 mL HF), followed by observation with an optical microscope (OM, Olumpus BX 60MF, Japan) and field-emission scanning electron microscope (FE-SEM, Hitachi 4800, Japan). The microstructural phases in the Ti - 30Nb - xTa alloys were identified with the aid of an X-ray diffractometer (XRD, X'Pert Pro, Philips, The Netherlands), utilizing Cu Kαradiation. The XRD peaks were identified using the JCPDS (Joint Committee on Power Diffraction Standards) diffraction data for element standards.

3.3. Si-HA deposited Ti-30Nb-xTa alloys

When the electrochemical deposition of Si-HA was carried out Ti-30Nb-xTa alloys surface without anodization treatment, the resultant coating was not uniform. Electrochemical deposition of Si-HA was conducted at 85 ℃ in modified simulated body fluid (M-SBF). The electrolyte was composed 2.5 mM $Ca(NO_3)_2 \cdot 4H_2O$ + 1.4 mM $NH_4H_2PO_4$ + 0.1 mM $Na_2SiO_3 \cdot 9H_2O$. Cyclic voltammetry (CV) studies were carried out applying in electrolytes in order to determine the parameters for electrochemical deposition and understand the electrochemistry of the deposition. CV was carried out at 85 ℃ using the above described three electrode configuration by scanning the potential between 0 V to -1.5 V at 100 mV/s for 10 cycles and 30 cycles using potentiostat/galvanostat (EG&GCo., 2273, USA). The pulsing cycle is schematically illustrated in Fig. 7. Also, the electrodeposition condition of Si-HA deposited surface are summarized in Table 7.

The surface morphology and chemical composition was observed with a FE-SEM and energy dispersive X-ray spectroscopy (EDS, Oxford ISIS 310, England). The crystal phase of the deposit was examined using a thin film X-ray diffractometer (TF-XRD, X'Pert Pro, Philips, Netherlands). TF-XRD analysis is done using a XRD with Cu Kα incident radiation. Attenuated total reflection fourier transform infrared (ATR-FTIR, FT/IR-4100, Jasco, Japan) spectroscopy also was performed to determine Si-HA stoichiometry deviations.

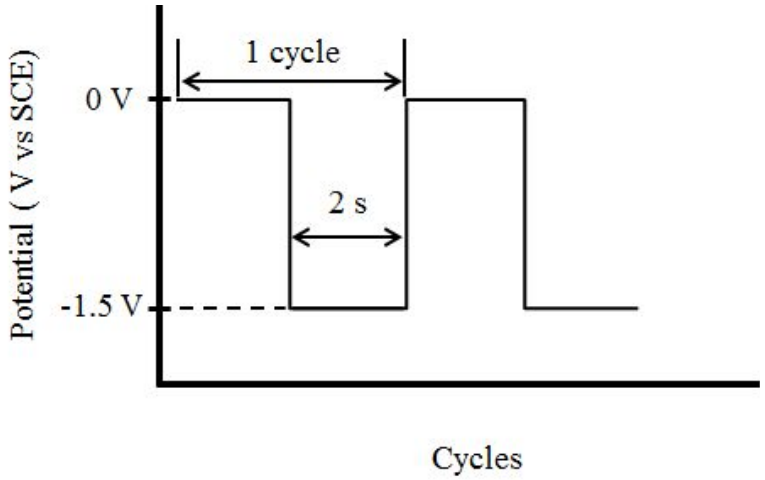

Fig. 4. Process of monitoring voltage versus cycles during the formation of Si-HA deposition.

Table 7. The condition of Si-HA deposition

	Cyclic voltammetry (CV)
Working electrode	Sample
Reference electrode	Saturated calomel electrode
Counter electrode	Pt
Electrolyte	2.5 mM $Ca(NO_3)_2 \cdot 4H_2O$ + 1.4 mM $NH_4H_2PO_4$ + 0.1 mM $Na_2SiO_3 \cdot 9H_2O$
Working temp.	85 ± 1 ℃
Scan rate	100 mV/s
Deposition cycles	10, 30

3.4. Surface wettability test of Si-HA deposited Ti-30Nb-xTa alloys

Surface wettability test was performed on the polished surface, Si-HA deposited surface using a water contact angle goniometer (Kruss DSA100, Germany) in sessile drop mode with 5 $\mu\ell$ drops.

Ⅳ. RESULTS AND DISCUSSION

4.1. Microstructures of Ti-30Nb-xTa alloys

Figure 8 shows the microstructures of the Ti-30Nb-xTa alloys with different Ta contents of 0, 3, and 15 wt. %, respectively. Fig. 8 (a) to (c) show the results of OM, and (d) to (f) show the results of FE-SEM for each group. In Fig. 8 (d), the martensitic phase (α″) in the equiaxed β-phase structure is designated by the arrow, and going to (b) and (c), it can be seen that the martensitic structure gradually disappeared with increasing Ta content. Also, the grain size increased as the Ta content increased. These results can be explained by a slight increase in volume fraction of the β phase, whereas the amount of α″ martensitic phase decreased with increasing Ta content. Also, these results show that Ta can decrease the martensitic start transformation temperature to below room temperature for the Ti-30Nb-15Ta alloy system [35-38].

Figure 9 shows the XRD patterns of the homogenized Ti-30Nb-xTa alloys. The XRD peaks were identified using the JCPDS diffraction data for element standards. Most peaks of Ti-30Nb-xTa alloy system corresponded to the α″ martensitic phase and bcc β phase. In the case of (a) the Ti-30Nb alloy, the XRD pattern shows higher intensity of the β-phase (110) peak at the 2-theta diffraction angle near 38.5 degrees and lower intensity of the β-phase (200) peak near 55.5 degrees. The Ti-30Nb surface also shows small peaks from the α″ phase for the (110), (020), (021), (130), (113), and (202) atomic planes. For the addition of 3 wt. % Ta to the alloy composition, the XRD pattern in (b) for Ti-30Nb-3Ta is similar to (a) for Ti-30Nb, but the α″ peaks had lower intensity than for (a), especially the α″ (110) peak near 34 degrees which has nearly disappeared. When the Ta content was increased to 15 wt. %, as shown in (c) for the Ti-30Nb-15Ta alloy, most of the XRD peaks were from the β

-phase, with reduced intensity of the α″ peaks. The intensity of the (200) β -phase peak was higher for the for the Ti-30Nb-15Ta alloy than for the (a) Ti-30Nb and (b) Ti-30Nb-3Ta alloys. The XRD results in Fig. 9, showing a decrease in intensity of the martensite α″ phase peaks with increased dominance of the β-phase peaks as the Ta content increases, are entirely matched with the microstructures revealed by OM and FE-SEM shown in Fig. 8. The present results confirm that the 3 wt. % and 15 wt. % Ta additions to the Ti-30Nb alloy decrease the amount of martensitic structure and increase the amount of transformation to β phase in Ti-30Nb-xTa alloy system. The lower elastic modulus of Ti-30Nb-15Ta alloy thus corresponds to a small portion of α″ phase and large portion of β phase in the microstructure that cannot induce martensitic transformation [37-39].

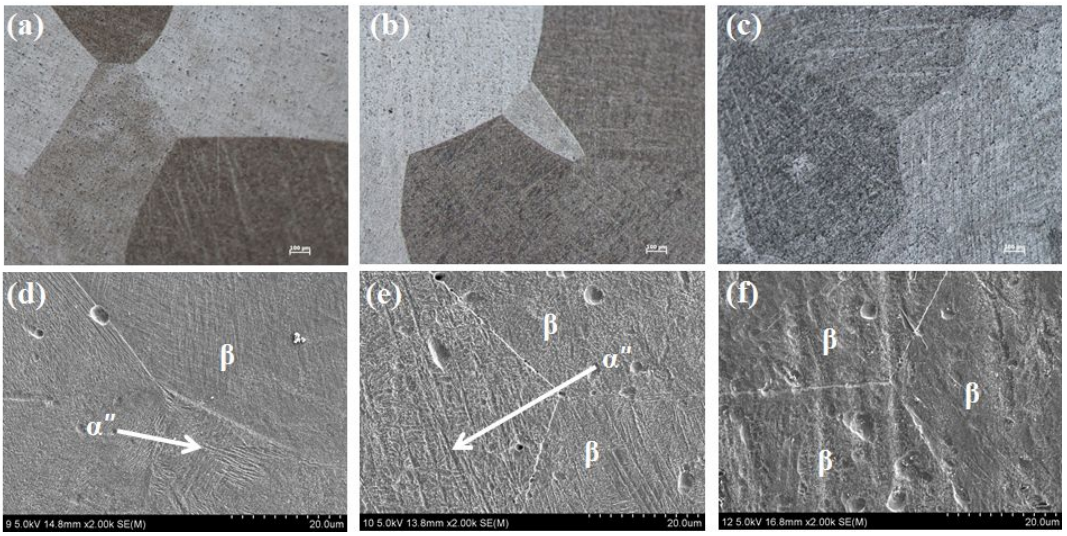

Fig. 5. Micrographs obtained with optical microscope (a, b, and c) and FE-SEM (d, e, and f) showing microstructures of heat-treated Ti-30Nb-xTa alloys: Ti-30Nb (a: x50, d: x2000), Ti-30Nb-3Ta (b: x50, e: x2000), Ti-30Nb-15Ta (c: x50, f: x2000)

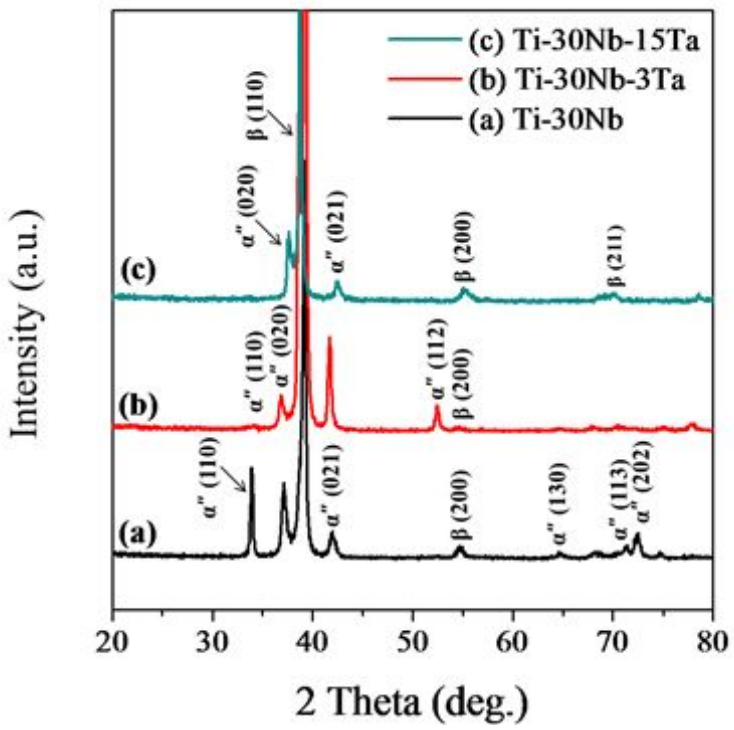

Fig. 6. XRD patterns for the homogenized Ti-30Nb-xTa alloys: (a) Ti-30Nb, (b) Ti-30Nb-3Ta, (c) Ti-30Nb-15Ta

4.2. Morphology of Si-HA deposited Ti-30Nb-xTa alloys

Figure 10 and 11 shows FE-SEM micrographs of the Si-HA deposited Ti-30Nb-xTa alloys for 10 and 30 cycles by electrochemical deposition. Fig. 10 (a) to (f) shows the low magnification of Si-HA deposited Ti-30Nb-xTa alloys surface, and Fig. 11 (a) to (f) shows the high magnification of Si-HA deposited Ti-30Nb-xTa alloys surface. In case of Fig. 10 and 11 (a), (b), and (c), shows the morphology of Si-HA deposited Ti-30Nb, Ti-30Nb-3Ta, and Ti-30Nb-15Ta alloys surfaces for 10 cycles, respectively. The images of Fig. 10 and 11 (d), (e), and (f) shows the morphology of Si-HA deposited Ti-30Nb, Ti-30Nb-3Ta, and Ti-30Nb-15Ta alloys surfaces for 30 cycles, respectively. Fig. 11 (a), (b), and (c) showed the plate-like structures in the range of low deposition cycles. On the other hand, Fig. 11 (d), (e), and (f) showed the flower-like and rod-like morphologies of Si-HA deposited Ti-30Nb, Ti-30Nb-3Ta and Ti-30Nb-15Ta alloys for 30 cycles, respectively. It is assumed that nucleation and growth of Si-HA depend on morphology of substrate and microstructure of alloy. In the case of a bulk surface of Ti-6Al-4V alloy, HA nucleation can more easily occur at β phase sites than at α phase sites, and HA nuclei that form at β phase sites grow rapidly and spread with diminishing surface energy, eventually having the plate-like HA morphology [40]. From pre-researched report [40], HA shape on bulk surface showed the keen plate-like deposits compared to Si-HA deposit. Therefore, Si-HA in the Ti-30Nb-xTa alloy was firstly precipitated and grown along the needle-like structure (martensitic structure) as shown in Fig. 8. And then Si-HA morphology was changed to dull plate-like shape with deposition cycles. There is not significantly different morphology according to alloying elements. The morphology of Si-HA on the bulk surface was changed with depending on the deposition cycles. As shown in Fig. 11 (d), (e), and (f), the plate-like structures were changed to mixed rod-like shapes and flower-like shape in Ti-30Nb-xTa alloy surface, and then finally changed to rod-like structure with increasing electrochemical deposition cycles up to 30 cycles. It

was previously reported that the crystal with the longitude direction of [002], and the six surfaces of the rod-like structures are (100) [41-43]. Therefore, particle size was nucleated and grown with broaden direction than one way direction as deposition cycles increased. Also, the results indicated that the amounts and morphology of deposits were major influenced by the electrolyte concentration and current density [44, 45].

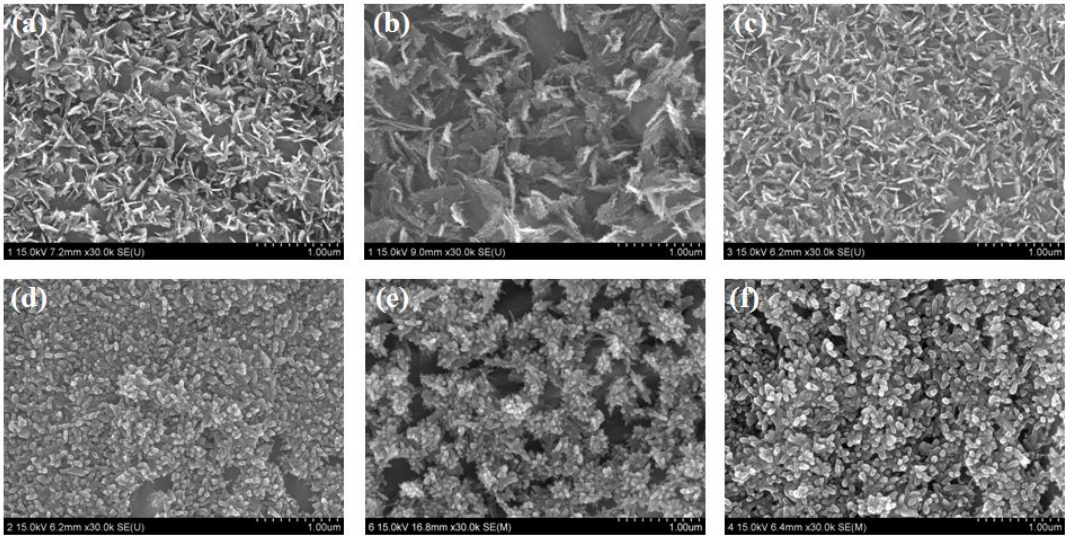

Fig. 7. FE-SEM images of Si-HA deposited Ti-30Nb-xTa alloys at low magnification: (a) Ti - 30Nb alloy for 10 cycle, (b) Ti - 30Nb-3Ta alloy for 10 cycle, (c) Ti - 30Nb - 15Ta alloy for 10 cycle, (d) Ti-30Nb alloy for 30 cycle, (e) Ti-30Nb-3Ta alloy for 30 cycle, (f) Ti-30Nb-15Ta alloy for 30 cycle

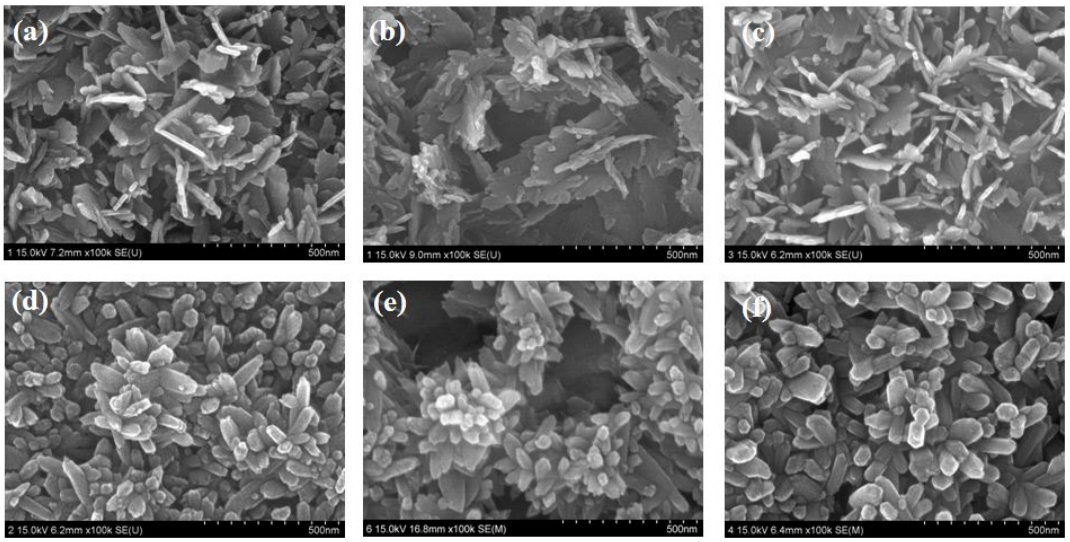

Fig. 8. FE-SEM images of Si-HA deposited Ti-30Nb-xTa alloys at high magnification: (a) Ti - 30Nb alloy for 10 cycle, (b) Ti - 30Nb-3Ta alloy for 10 cycle, (c) Ti - 30Nb - 15Ta alloy for 10 cycle, (d) Ti-30Nb alloy for 30 cycle, (e) Ti-30Nb-3Ta alloy for 30 cycle, (f) Ti-30Nb-15Ta alloy for 30 cycle

4.3. Surface properties of Si-HA deposited Ti-30Nb-xTa alloys

Figure 12 shows the EDS results for the chemical composition analyses of Si-HA deposited Ti-30Nb-xTa alloys for 10 and 30 cycles. The EDS result of Si-HA deposited Ti-30Nb alloy with deposition cycles are presented in Fig. 12 (a) and (b), and the EDS result of Si-HA deposited Ti-30Nb-3Ta alloy with deposition cycles are presented in Fig. 12 (c) and (d). In addition, the images of Fig. 12 (e) and (f) shows the Si-HA deposited Ti-30Nb-15Ta alloy with deposition cycles. From the EDS results, Si-HA deposited Ti-30Nb-xTa alloys consisted of O, Si, Ca, and P in all coated samples. These results indicated that the coatings were successfully deposited Ti-30Nb-xTa alloys. The present results suggest that the chemical composition of Si-HA coating confirmed the new bone tissue and the Ti substrate [46].

Figure 13 shows the TF-XRD results of Si-HA on the Ti-30Nb (a), Ti-30Nb-3Ta (b) and Ti-30Nb-15Ta (c) alloys. Each peaks matches the HA and β-Ti peak. The peaks of the HA were showed ranging from 20° to 45° for 2 theta. The four strong intensity of HA peaks are showed 25.9, 31.7, 32.1, and 32.8° 2 theta dominates the diffraction peaks. In case of Ti-30Nb-15Ta (c) alloy, the HA peaks were disappeared, whereas the intensity of the HA and β-Ti peak predominantly increased. It was also found that the HA peak at the 2 theta degree of around 25.9, exhibiting an orientation to the c-axis direction of the HA crystal [47, 48].

Figure 14, 15, and 16 shows the ATR-FTIR results for Si-HA deposited Ti-30Nb-xTa alloys for various deposition cycles (10 and 30 cycles) obtained by electrochemical deposition. The ATR-FTIR was used to investigate the effect of the Si substitution on the phosphate and hydroxyl bands of HA structure. As shown in Fig. 14, 15 and 16, a weak OH band at 3570 cm^{-1} was obscured by abroad band between 3200 and 3600 cm^{-1}, which is characteristic of moisture in the sample [11, 49-50]. Intense bands at 1031 and 1025 cm^{-1} can

be observed, which correspond to P-O stretching band, as shown in Fig. 14, 15, and 16. As deposition cycles increased, the P-O stretching bands shifts from 1114 cm^{-1} to 1025 cm^{-1}. This result indicated that the Si was most notable influence on the Si-HA deposition. The bands at 2387 cm^{-1} correspond to Si-HA and HA spectra [49, 50], however, the bands in Si-HA coating disappeared when the sample was heated at 800 ℃ for 6 h [51]. Our result suggests that the charge difference resulting from the substitution of SiO_4^{4-} for PO_4^{3-} in HA, is compensated by loss of OH^-, which is limited by the number of OH ions that can be extracted from the HA structure [52].

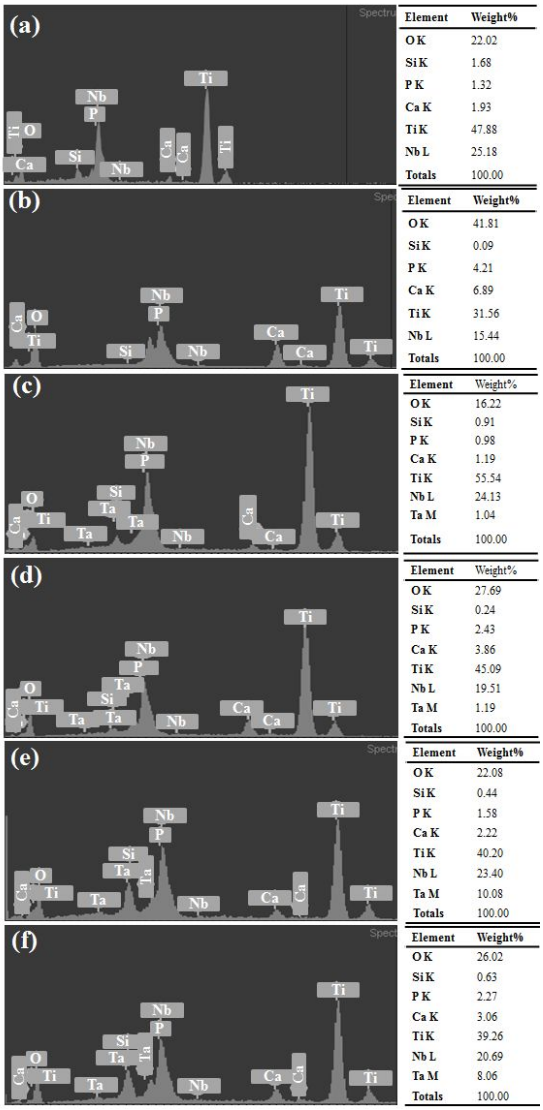

Fig. 9. EDS analysis of Si-HA deposited Ti-30Nb-xTa alloys: (a) Ti-30Nb alloy for 10 cycles, (b) Ti-30Nb alloy for 30 cycles, (c) Ti-30Nb-3Ta alloy for 10 cycles, (d) Ti-30Nb-3Ta alloy for 30 cycles, (e) Ti-30Nb-15Ta alloy for 10 cycles, (f) Ti-30Nb-15Ta alloy for 30 cycles

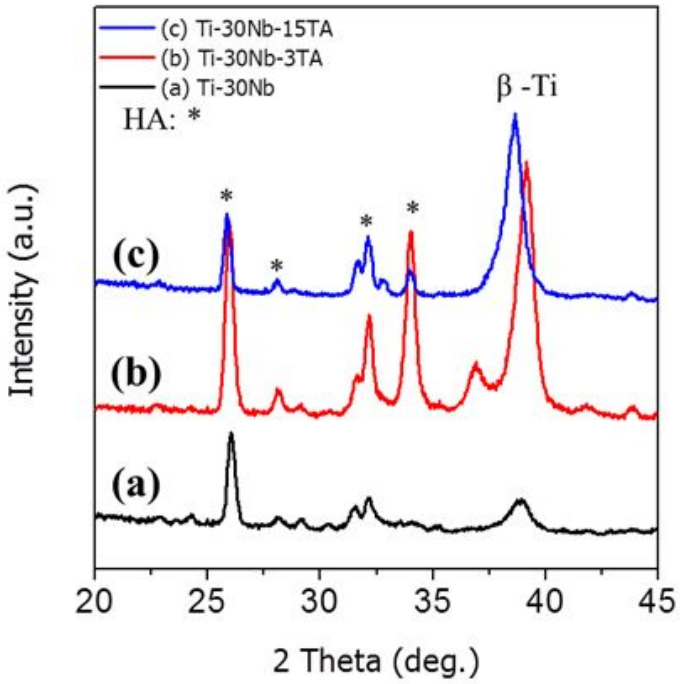

Fig. 10. TF-XRD peaks of Si-HA deposited Ti-30Nb-xTa alloys: (a) Ti-30Nb alloy, (b) Ti-30Nb-3Ta alloy, (c) Ti-30Nb-15Ta alloy

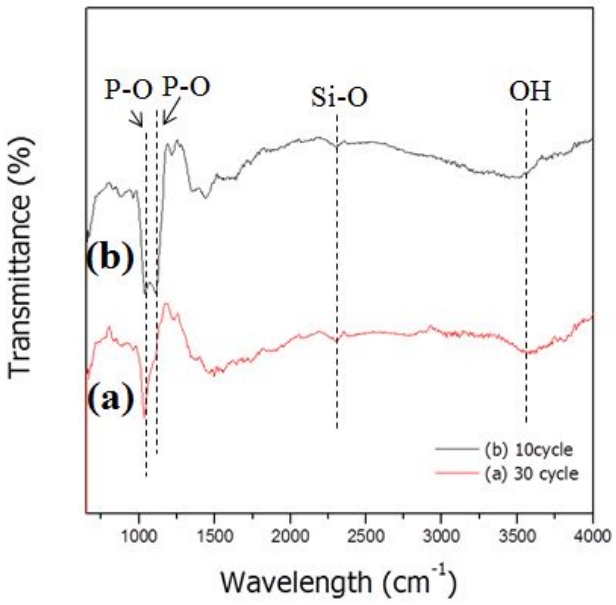

Fig. 11. ATR-FTIR spectra of Si-HA deposited Ti-30Nb alloys for 10 and 30 cycles: (a) 10 cycle, (b) 30 cycle

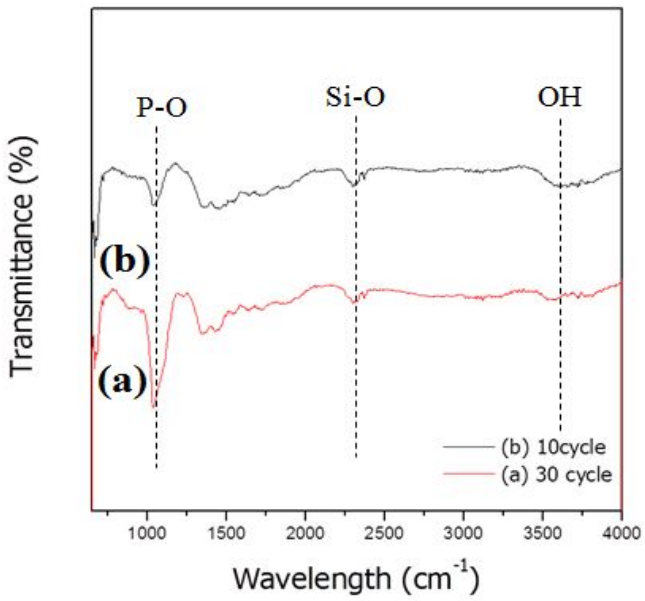

Fig. 12. ATR-FTIR spectra of Si-HA deposited Ti-30Nb-3Ta alloys for 10 and 30 cycles: (a) 10 cycle, (b) 30 cycle

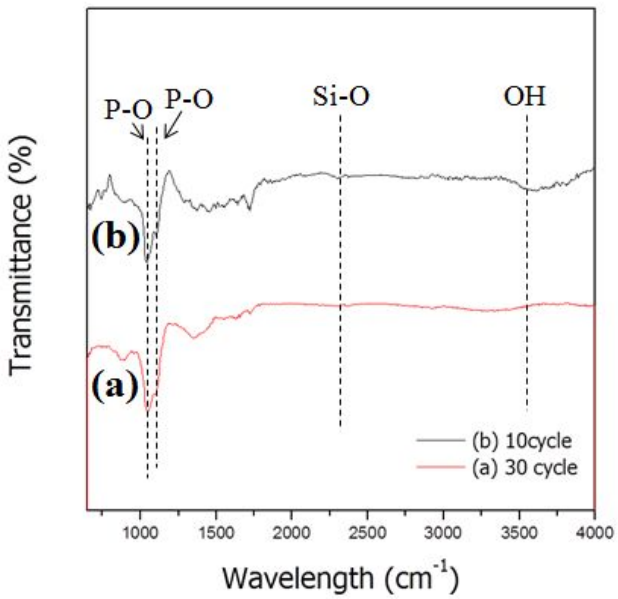

Fig. 13. ATR-FTIR spectra of Si-HA deposited Ti-30Nb-15Ta alloys for 10 and 30 cycles: (a) 10 cycle, (b) 30 cycle

4.4. Wettability of Si-HA deposited Ti-30Nb-xTa alloys with deposition cycles

Figure 17 shows the contact angle values of Ti-30Nb-xTa alloys with different surface treatments. Fig. 17 (a) to (c) shows the contact angle values of Si-HA deposited Ti-30Nb alloy with deposition cycles, whereas Fig. 17 (d) to (f) shows the contact angle values of Si-HA deposited Ti-30Nb-3Ta alloy with deposition cycles. Ti-30Nb-15Ta alloy [Fig. 17 (g) to (i)] shows the contact angle values of Si-HA deposition with deposition cycles. As the Ta content increased from 3 wt. % to 15 wt. %, the contact angles value of the polished surface showed in the order of around 55°, 58°, and 50°, respectively. In Fig. 17 (b), (e), and (h), the contact angles value of Si-HA deposited Ti-30Nb-xTa alloys for 10 cycle are observed around 32°, 36°, and 34°, respectively. Si-HA deposited Ti-30Nb-xTa alloys for 30 cycle value, such as around 26°, 24°, and 26°, were presented in Fig. 17 (c), (f), and (i). The corresponding contact angle value are shown in Table 8. The results indicated that the contact angles decrease in the order of polished, 10 cycles, and 30 cycles with significantly lower values of around 55° to 26°. From the wettability test results in Fig. 17, it is evident that the Si-HA deposited Ti-30Nb-xTa alloys for 30cycle [Fig. 17 (c), (f), and (i)] lower contact angle values compared to the polished Ti-30Nb-xTa alloys and Si-HA deposited Ti-30Nb-xTa alloys for 10 cycle. Generally, the Si-HA deposited Ti-30Nb-xTa alloys showed good wettability compared to the polished Ti alloy substrate. It is indicated that Si plays an active role in the cell attachment and proliferation [53]. These in vitro studies showed that the modification of the surface wettability and enhanced the early stage protein expression on the Si-HA surface [54].

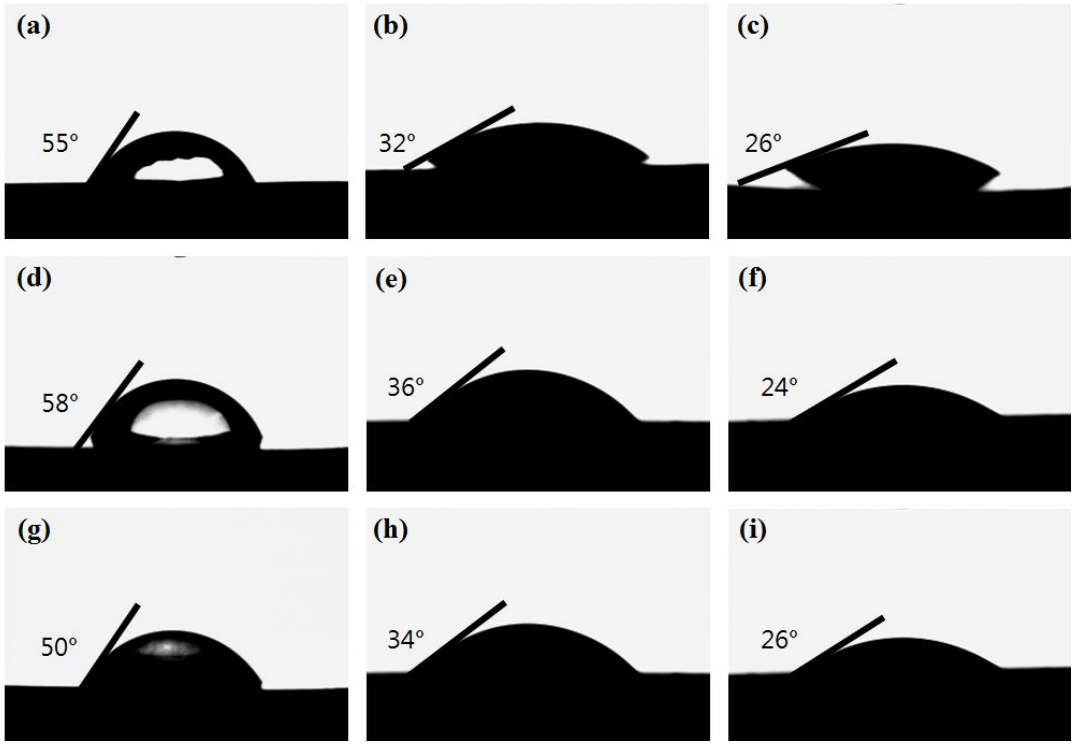

Fig. 14. The contact angle values of Si-HA deposited Ti-30Nb-xTa alloys with different treatments: (a) polished Ti-30Nb alloy, (b) Si-HA deposited Ti-30Nb alloy for 10 cycles, (c) Si-HA deposited Ti-30Nb alloy for 30 cycles, (d) polished Ti-30Nb-3Ta alloys, (e) Si-HA deposited Ti-30Nb-3Ta alloy for 10 cycles, (f) Si-HA deposited Ti-30Nb-3Ta alloy for 30 cycles, (g) polished Ti-30Nb-15Ta alloys, (h) Si-HA deposited Ti-30Nb-15Ta alloy for 10 cycles, (i) Si-HA deposited Ti-30Nb-15Ta alloy for 30 cycles

Table 8. Contact angle value of Si-HA deposited Ti-30Nb-xTa alloys

Sample	Polished	10 cycle	30 cycle
Ti-30Nb	55±2°	32±2°	26±1°
Ti-30Nb-3Ta	58±2°	35±1°	24±2°
Ti-30Nb-15Ta	50±1°	34±1°	26±1°

Ⅴ. CONCLUSIONS

In this study, surface characteristics of Si-HA film coated Ti-30Nb-xTa alloys by electrochemical deposition have been researched. The Ti-30Nb-xTa ingots were fabricated by using a vacuum arc melting furnace. The Ti-30Nb-xTa ingots were homogenized in a vacuum furnace for 12 h at 1000 ℃ in a Ar atmosphere, followed by quenching in 0 ℃ water. Silicon-substituted hydroxyapatite (Si-HA) coatings were prepared on Ti-30Nb-xTa alloys by electrochemical deposition technique in electrolytes containing Ca^{2+}, PO_4^{3-}, and SiO_3^{2-} ions. The surface characteristics of Si-HA deposited Ti-30Nb-xTa alloys has been researched by FE-SEM, EDS, XRD, FTIR, and wettability test.

The results were as follows;

1. Microstructural examination revealed that the grain size of the Ti-30Nb-xTa alloys increased as the Ta content increased. For the Ti-30Nb alloy without Ta, XRD revealed α″ martensite phase peaks with strong peaks of β phase, whereas for the two Ti-30Nb-xTa alloys an increase in Ta content caused the microstructure to change from α″ + β phase to solely β phase.
2. Si-HA in the Ti-30Nb-xTa alloy was firstly precipitated and grown along the needle-like structure (martensitic structure). The plate-like structures were changed to mixed rod-like and flower-like shapes, and then finally changed to rod-like structure. The morphology of Si-HA on the bulk surface was changed with depending on the deposition cycles.
3. From the EDS results, Si-HA deposited by electrochemical deposition on the Ti-30Nb-xTa alloys surface had a chemical composition consisted of O, Ca, P, Si, Ti, Nb, and Ta. The phase of Si-HA deposited Ti-30Nb-xTa alloys were identified to be Si-HA structures elongated parallel to the c-axis direction. From ATR-FTIR spectra, Si existed in the form of SiO_4^{4-}

groups in Si-HA coating.

4. The contact angles of Si-HA deposited Ti-30Nb-xTa alloys for 30 cycles had the lower than those of others and good wettability for biocompatibility.

In conclusion, there is evidence that the morphology of Si-HA on the bulk surface was changed with depending on the deposition cycles. Si-HA deposited Ti-30Nb-xTa alloys for 30 cycle surface shows a hydrophilic behavior. These findings suggest that Si-HA is an improved bioactivity for biomaterials.

- Reference -

1. S. Sahu, M. Palaniappa, S.N. Paul, M. Roy, Mater. Lett. 64 (2010) 12.
2. L. Thair, U.K. Mudai, S. Rajagopalan, R. Asokamani, B. Raj, Corros. Sci. 45 (2003) 1951.
3. H.Y. Kim, S. Hashimoto, J.I. Kim, T. Inamura, H. Hosoda, S. Miyazaki, Mater. Sci. Eng., A 417 (2006) 120.
4. X.M. Ma, W. Sun, J. Alloys Compd. 509S (2011) S294.
5. M. Abdel-Hady, H. Fuwa, K. Hinoshita, H. Kimura, Y. Shinzato, M. Morinaga, Scr. ater. 57 (2007) 1000.
6. M. Abdel-Hady, K. Hinoshita, M. Morinaga, Scr. ater. 55 (2006) 477.
7. S.F. Ou, C.S. Lin, Y.N. Pan, Surf. Coat. Thechnol. 205 (2011) 2899.
8. E.S. Kim, Y.H. Jeong, H.C. Choe, J. Nanosci. Nanotechnol. (2013), doi:10.1166/jnn.2013.8389.
9. K. Fatehi, F. Moztarzadeh, M.S. Hashjin, M. Tahriri, M. Rezvannia, R. Ravarian, Bull. Mater. Sci. 31 (2008) 101.
10. D.M. Ibrahim, A.A. Mostafa, S.I. Korowash, Chem. Cent. J. 5 (2011) 74.
11. Th. Leventouri, C.E. Bunaciu, V. Perdikatsis, Biomater. 24 (2003) 4205.
12. S. Cheng, D. Wei, Y. Zhou, H. Guo, Ceram. Int. 37 (2011) 2505.
13. D. Marchat, M. Zymelka, C. Coelho, L. Gremillard, L.J. Pottuz, F. Babonneau, C. Esnouf, J. Chevalier, D.B. Assollant, Acta Biomater. 9 (2013) 6992.
14. Q. Tang, R. Brook, N. Rushton, M. Best, J. Mater. Med. 21 (2010) 173.
15. E. Zhang, C. Zou, G. Yu, Mater. Sci. Eng., C 29 (2009) 298.
16. E. Thian, J. Huang, M. Vickers, S. Best, Z. Barber, W. Bonfield, J. Mater. Sci. 41 (2006) 709.
17. N. Hijon, M. Cabanas, J. Pena, M. Vallet-Regi, Acta Biomater. 2 (2006) 567.
18. Y.H. Jeong, H.C. Choe, W.A. Brantley, I.B. Sohn, Surf. Coat. Thechnol. 217 (2013) 13.
19. M. McCracken, D.S.S, M.S.B.E, J. Prosthodont. 8 (1999) 40.

20. C. Leyens, M. peters (Ed.), Titanium and Titanium Alloys, Fundamentals and Applications, Wiley-VCH GmbH & Co. KGaA, Weinheim, Germany, 2003, pp. 1-4.
21. M. Geetha, A.K. Singh, R. Asokamani, A.K. Gogia, Gogia, Prog. Mater. Sci. 54 (2009) 397.
22. P.G. Liang Jr, E.S. Ferguson Jr, E.S. Hodge, J. Biomed. Mater. Res. 1 (1967) 135.
23. P. Bania, D. Eylon et al. (eds.), Beta Titanium Alloys and Their Role in the Titanium Industry, in: Beta Titanium Alloys in the 1990's, TMS, Warrendale, PA, USA, 1993, pp. 6.
24. Y. Song, D.S. Xu, R. Yang, D. Li, W.T. Wu, Z.X. Guo, Mater. Sci. Eng. A 260 (1999) 269.
25. N. Sakaguchi, M. Niinomi, T. Akahori, J. Takeda, H. Toda, Mater. Sci. Eng. C 25 (2005) 363.
26. S. Hanada, T. Ozaki, T. Watanabe Takahashi, K. Yoshimi, T. Abumiya, Mater. Sci. Forum. 426-432 (2003) 3103.
27. S.J. Li, R. Yang, S. Li, Y.L. Hao, Y.Y. Cui, M. Niinomi, Wear 257 (2004) 869.
28. K. Duan, R. Wang, J. Mater. Chem. 16 (2006) 2309.
29. E. Boanini, M. Gazzano, A. Bigi, Acta Biomater. 6 (2010) 1882.
30. A. Kar, K.S. Raja, M. Misra, Surf. Coat. Thechnol. 201 (2006) 3723.
31. S.V. Dorozhkin, M. Epple, Angew. Chem. Int. Ed. 41 (2002) 3130.
32. M. Vallet-Regi, D. Arcos, J. Mater. Chem. 15 (2005) 1509.
33. A.E. Porter, N. Patel, J.N. Skepper, S.M. Best, W. Bonfield, Biomater. 24 (2003) 4609.
34. Z.Y. Qiu, I.S. Noh, S.M. Zhang, Front. Mater. Sci. 7 (2013) 40.
35. A.M. Pietak, J.W. Reid, M.J. Stott, M. Sayer, Biomater. 28 (2007) 4023.
36. E. Zhang, C. Zou, S. Zeng, Surf. Coat. Thechnol. 23 (2009) 1075.
37. D.Y. Lin, X.X. Wang, Surf. Coat. Thechnol. 204 (2010) 3205.
38. P. R. Rios, F. Siciliano Jr., H. R. Z. Sandim, R. L. Plaut, A. F. Padiha, Mater. Res. 8 (2005) 225.

39. M. Niinomi, Mater. Sci. Eng. A243 (1998) 231.
40. H. Y. Kim, S. Hashimoto, J.I. Kim, T. Inamura, H. Hosoda, S. Miyazaki, Mater. Sci. Eng. A 417 (2006) 120.
41. E.S. Kim, Y.H. Jeong, H.C. Choe, W.A. Brantley, Thin Solid Films 549 (2013) 141.
42. W. G. Kim, H. C. Choe, W. A. Brantley, Thin Solid Films 519 (2011) 4633.
43. C.I. Jo, Y.H. Jeong, H.C. Choe, W.A. Brantley, Thin Solid Films 549 (2013) 135.
44. D.H. Li, J. Lin, D.Y. Lin, X.X. Wang, J. Mater. Sci. Mater. Med. 22 (2011) 1205.
45. M. Ma, W. Ye, X.X. Wang, Mater. Lett. 62 (2008) 3875.
46. W. Ye, X.X. Wang, Mater. Lett. 61 (2007) 4062.
47. Y.H. Jeong, H.C. Choe, W.A. Brantley, J. Mater. Sci. Mater. Med. 22 (2011) 41.
48. S. Roessler, R. Born, D. Scharnweber, H. Worch, A. Sewing, M. Dard, J. Mater. Sci. Mater. Med. 12 (2001) 871.
49. E. Zhang, C. Zou, Acta Biomater. 5 (2009) 1732.
50. K. Lee, Y.M. Ko, H.C. Choe, B.H. Kim, J. Nanosci. Nanotechnol. 12 (2012) 822.
51. K. Lee, B.H. Moon, Y.M. Ko, H.C. Choe, Surf. Interface Anal. 44 (2012) 1492.
52. R.L. Williams, M.J. Hadley, P.J. Jiang, N.A. Rowson, P.M. Mendes, J.Z. Rappoprt, M. Grover, J. Mater. Chem. 1 (2013) 4370.
53. E. Zhang, C. Zou, S. Zeng, Surf. Coat. Technol. 203 (2009) 1075.
54. X. Lian, X.F. Xiao, R.F. Liu, Mater. Lett. 59 (2005) 3841.
55. D.M. Ibrahim, A.A. Mostafa, S.I. Korowash, Chem. Cent. J. 5 (2011) 74.
56. E. Zhang, C. Zou, G. Yu, Mater. Sci. Eng. C 29 (2009) 298-305.
57. E.S. Thian, Z. Ahmad, J. Huang, M.J. Edirisinghe, S.N. Jayasinghe, D.C. Ireland, R.A. Brooks, N. Rushton, W. Bonfield, S.M. Best, Acta Biomater. 6 (2010) 750-755.

감사의 글

어느 덧 2013년에도 첫눈이 오면서 겨울을 알리고 새해의 좋은 꽃을 피우기 위해 마지막을 마무리하는 시간이 왔습니다. 다사다난했던 2년이란 시간을 되짚어보니 어려운 영어논문 작성과 학회발표 준비를 하면서 서툴고 어려워서 조금은 힘들었지만, 포기하지 않고 끊임없이 지적 받은 것을 바탕으로 조금씩 수정해나가다 보니 이러한 좋은 결과를 얻을 수 있었던 것 같습니다. 이렇게 졸업논문을 마무리 하면서 제가 여기까지 달려오는데 도움을 주신 분들에게 감사의 마음을 전해보고 자 펜을 듭니다.

항상 저희에게 끊임없는 관심과 애정을 갖고 누구보다 아끼지 않는 조언을 해주시는 최한철 교수님께 감사하다는 마음을 전하고 싶습니다. 교수님, 항상 건강하시고 저희로 인해 갖고 있던 근심걱정을 내려놓으시고 새해에도 좋은 일만 가득하시길 기원하겠습니다. 그리고 항상 저의 안부를 물어주시며 졸업 후에서 좋은 말씀으로 저에게 힘이 되어 주셨던 강보안 교수님께도 감사의 마음을 전합니다. 또한 바쁘신 와중에도 시간을 내주어 논문을 지도 편달 해주신 장현선 교수님께도 감사드립니다.

미국에서 바쁘신 와중에도 저희에게 조언과 격려를 아끼지 않았던 용훈 오빠에게도 감사의 인사를 전하고 싶습니다. 늘 편하게 모르는 부분을 잘 가르쳐 주시는 강이 오빠, 신혼생활 잘하시길 바랍니다. 2년 동안 고생했던 성환 오빠와 현주 오빠 수고 많았고 앞으로 좋은 일만 가득하길 바랍니다. 항상 긍정적인 채익 오빠와 이번에 들어오게 될 인섭이와 김정재 선생님 열심히 해서 좋은 결과 있었으면 좋겠습니다.

마지막으로 멀리에서도 묵묵히 저의 길을 응원해 주신 부모님에게 깊이 감사드립니다. 부모님이 있어 포기하지 않고 열심히 여기까지 올 수 있었던 것 같습니다. 앞으로도 실망시키지 않고 열심히 노력하는 딸이 되겠습니다. 사랑합니다. 먼저 사회생활을 시작해서 힘들어도 내색하지 않는 밝은 여동생, 항상 고맙고 미안하고 감사하게 생각합니다. 지금 군복무로 누구보다 고생하고 있는 남동생, 몸조심하고 멋진 남자로 돌아오길 바랍니다. 우리집의 귀염둥이 막둥이! 게임 좀 줄이고 그 열정을 공부에 조금이나마 돌려보았으면 좋겠습니다.

다시 한 번 모든 분들께 감사드리며 항상 건강하시길 바랍니다.

저작물 이용 허락서

학 과	광기술공학과(광응용공학전공)	학 번	20127165	과 정	석사
성 명	한글: 김 은 실 한문 : 金 恩 實 영문 : Kim Eun-Sil				
주 소	광주광역시 동구 서석동 423-6 명은빌라 304호				
연락처	E-MAIL : dmsry0136@hanmail.net				
논문제목	한글 : 전기화학증착법을 이용하여 Si-HA가 증착된 Ti-30Nb-xTa 합금의 표면특성 영어 : Surface Characteristics of Si-HA Film Coated Ti-30Nb-xTa Alloys by Electrochemical Deposition				

본인이 저작한 위의 저작물에 대하여 다음과 같은 조건아래 조선대학교가 저작물을 이용할 수 있도록 허락하고 동의합니다.

- 다 음 -

1. 저작물의 DB구축 및 인터넷을 포함한 정보통신망에의 공개를 위한 저작물의 복제, 기억장치에의 저장, 전송 등을 허락함
2. 위의 목적을 위하여 필요한 범위 내에서의 편집·형식상의 변경을 허락함. 다만, 저작물의 내용변경은 금지함.
3. 배포·전송된 저작물의 영리적 목적을 위한 복제, 저장, 전송 등은 금지함.
4. 저작물에 대한 이용기간은 5년으로 하고, 기간종료 3개월 이내에 별도의 의사 표시가 없을 경우에는 저작물의 이용기간을 계속 연장함.
5. 해당 저작물의 저작권을 타인에게 양도하거나 또는 출판을 허락을 하였을 경우에는 1개월 이내에 대학에 이를 통보함.
6. 조선대학교는 저작물의 이용허락 이후 해당 저작물로 인하여 발생하는 타인에 의한 권리 침해에 대하여 일체의 법적 책임을 지지 않음
7. 소속대학의 협정기관에 저작물의 제공 및 인터넷 등 정보통신망을 이용한 저작물의 전송·출력을 허락함.

동의여부 : 동의(O) 반대( )

2014 년 02 월 25 일

저작자: 김 은 실 (서명 또는 인)

조선대학교 총장 귀하